

## Full Length Article

# Microstructure characterization and grain morphology of alloy 625 with 0.4 wt% boron modification manufactured by laser wire deposition

Y. Tian, N. Chekir, X. Wang, A. Nommeots-Nomm, R. Gauvin, M. Brochu\*

Department of Mining and Materials Engineering, McGill University, 3610 University Street, Wong Building, Montreal, Quebec, H3A 0C5, Canada

## ARTICLE INFO

## Keywords:

Alloy 625  
Laser wire deposition  
Microstructure characterization  
Grain morphology  
Rapid solidification

## ABSTRACT

Laser wire deposits using Alloy 625 modified with 0.4 wt% B were manufactured on stainless steel 304 substrates. A layer boundary with a thickness of around 250  $\mu\text{m}$  was formed between the layer cores during deposition. Results show that the solidification features in the layer boundary were coarser than the layer core due to the recalescence mechanism. Continuous eutectics were observed segregating the inter-dendritic regions in both the layer boundary and the layer core. The eutectics consisted of mainly Laves phase with a small amount of NbC precipitates. Solidification front velocities (SFV) were calculated from the Kurz-Giovanola-Trivedi (KGT) model. Results showed that they developed in the layer boundary and in the layer core at 0.06 m/s and 0.1 m/s respectively. Electron backscattered diffraction (EBSD) mapping revealed that small equiaxed grains nucleated in the layer boundary, while large columnar grains were prevalent in the layer core. Pole figures showed a strong oriented texture was present along the (100) plane. The columnar to equiaxed transition (CET) model developed by Hunts was considered and the results were in good agreement with the observed grain morphologies.

## 1. Introduction

Alloy 625 is one type of solid solution strengthening Ni-based superalloys hardened via the inclusion of refractory elements including Mo and Nb [1–3]. Alloy 625 is usually applied to repair the damage sustained in Ni-based superalloy gas turbine vanes and blades due to its excellent combination of weldability, tensile properties, and corrosion resistance in aggressive chemical environments and at high temperatures [4–8]. The laser wire deposition process belongs to the family of direct energy deposition processes and uses a high energy density laser to fuse a filler wire to a substrate in order to form the deposition. As a rapid solidification layer-by-layer laser additive manufacturing (LAM) technology, this process has the capability to not only re-build the damaged part with little distortion or dilution, but can also produce net shape constructions of complicated geometries without the need for significant post treatment [9]. Therefore, the laser wire deposition technique is drawing more and more momentum for the repair of damaged gas turbine components.

Recently, research on LAM processing of Alloy 625 has been published [10–14]. Abioye et al. [11] manufactured samples via laser wire deposition with low contact angle, minimal dilution ratio and high surface quality as a function of processing parameters, giving special attention to the energy per unit length of track. Dinda et al. [10]

investigated the microstructural evolution and thermal stability of samples fabricated by laser powder deposition, and concluded that the microstructure in the as-deposited condition consisted mostly of columnar dendrites with epitaxial growth from the substrate. Li et al. [14] work reported upon the microstructure of samples produced via selective laser melting (SLM), and observed that the texture of the material was mainly along (100) planes with epitaxial grain growth. Although the aforementioned papers discuss the different attributes of AM produced parts they only consider the traditional Alloy 625 composition.

It is known that when repairing  $\gamma'$  Ni-based superalloy components, the base metal suffers from hot cracks during solidification [15–17] and strain-age cracks during heat treatment [17]. Alexandrov et al [18] reported that the cracks could be healed via backfilling if sufficient eutectic volume was formed during terminal solidification. They studied the weldability of nickel-based superalloys with different compositions and found evidence of crack healing via backfilling of eutectics when using high Nb filler alloys [18]. One method to achieve higher amounts of eutectics is to add boron additions to the Alloy 625 composition. This methodology has been validated in previous work, where the eutectic amount was increased from around 2 vol.% in conventional Alloy 625 to 12 vol.% in the 0.4 wt% B modified Alloy “625B” during gas tungsten arc deposition [19].

In this work we investigated the Alloy 625 modified with 0.4 wt% B

\* Corresponding author.

E-mail address: [mathieu.brochu@mcgill.ca](mailto:mathieu.brochu@mcgill.ca) (M. Brochu).

**Table 1**  
Chemical composition of 625B wires used for gas tungsten arc deposition builds, wt%.

	Ni	Fe	Nb	Mo	Cr	Al	Ti	Co	Mn	Si	B	C
625B	balanced	–	3.7	9	21	0.4	0.4	1	–	–	0.4	0.02

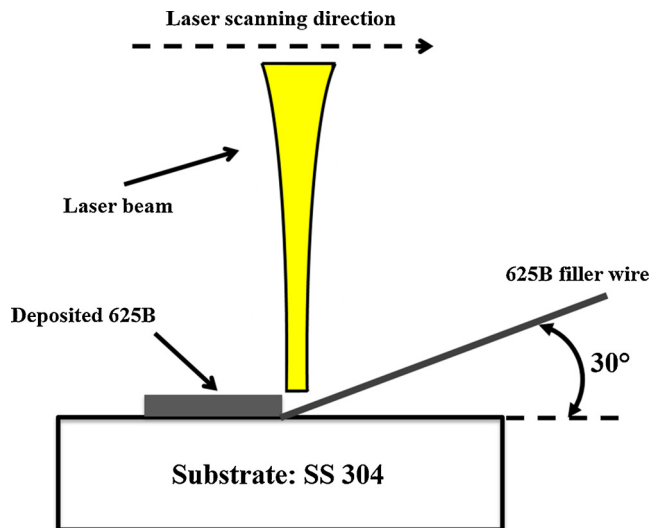


**Fig. 1.** Schematic drawing of laser wire deposition process using 625B wire on a stainless steel 304 substrate.

to see if the eutectic volume could be further increased and utilized to backfill cracks formed during laser wire deposition. It is known that microstructure and grain morphology determine the mechanical properties and final performance of the built part. Normally during additive manufacturing columnar grains are formed during deposition due to epitaxial grain growth [20]. However, due to variation of the thermal gradient and cooling rate, different grain morphologies could be developed, which would lead to different mechanical properties [21]. Thus, in the current research, microstructure characterization, rapid solidification behavior and grain morphology during the deposition process were investigated.

## 2. Experimental procedure

Samples for the current study were produced by Liburdi Turbine Service. Laser wire deposits of Alloy 625 wires containing 0.4 wt% B (referred to as 625B) were conducted on a stainless steel 304 substrate. The chemical composition of 625B wires is presented in Table 1. This chemical composition was confirmed by both a Thermo Scientific™ ELEMENT 2™ inductively coupled plasma- mass spectrometry (ICP-MS) and a JEOL 8900 Electron Probe Microanalysis (EPMA) tests. A schematic drawing of the laser wire deposition process performed is shown in Fig. 1. Ten layers of deposits were built upon the substrate, with approximately dimensions of 20 mm in height, 3 mm in width, and 50 mm in length. The samples were produced using a LAWS 1000 automated deposition system. The robot was controlled by the WinLAWS system. An IPG Yb:YAG fiber laser (IPG Photonics, Oxford) reaching up to 1 kW power was used to fuse the material. During deposition, the laser beam power used was 800 W; the wire feed rate was kept at 150 mm/min; the laser beam spot size was around 1 mm; and the defocusing distance was around 12 cm. Argon was employed as a shielding gas during the deposition procedure.

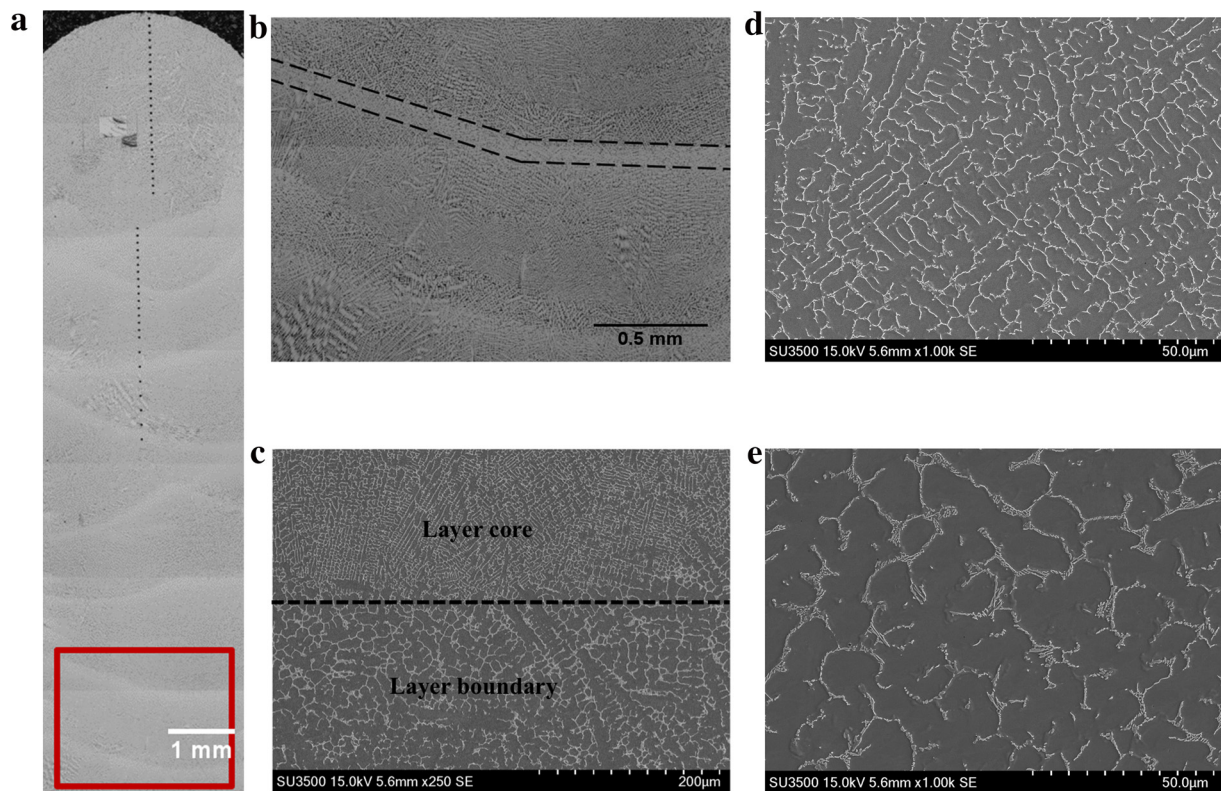


**Fig. 2.** (a). Macroscopic image of as-deposited sample (Fig. 2b is taken from the region in red square); (b). Optical microscope image of as-deposited sample showing clear layer boundary with thickness of around 250 μm; (c). SEM micrograph indicating larger features in the layer boundary than the layer core; (d). Higher magnification SEM micrograph of the layer core and (e) of the layer boundary (For interpretation of the references to colour in this figure legend, the reader is referred to the web version of this article).

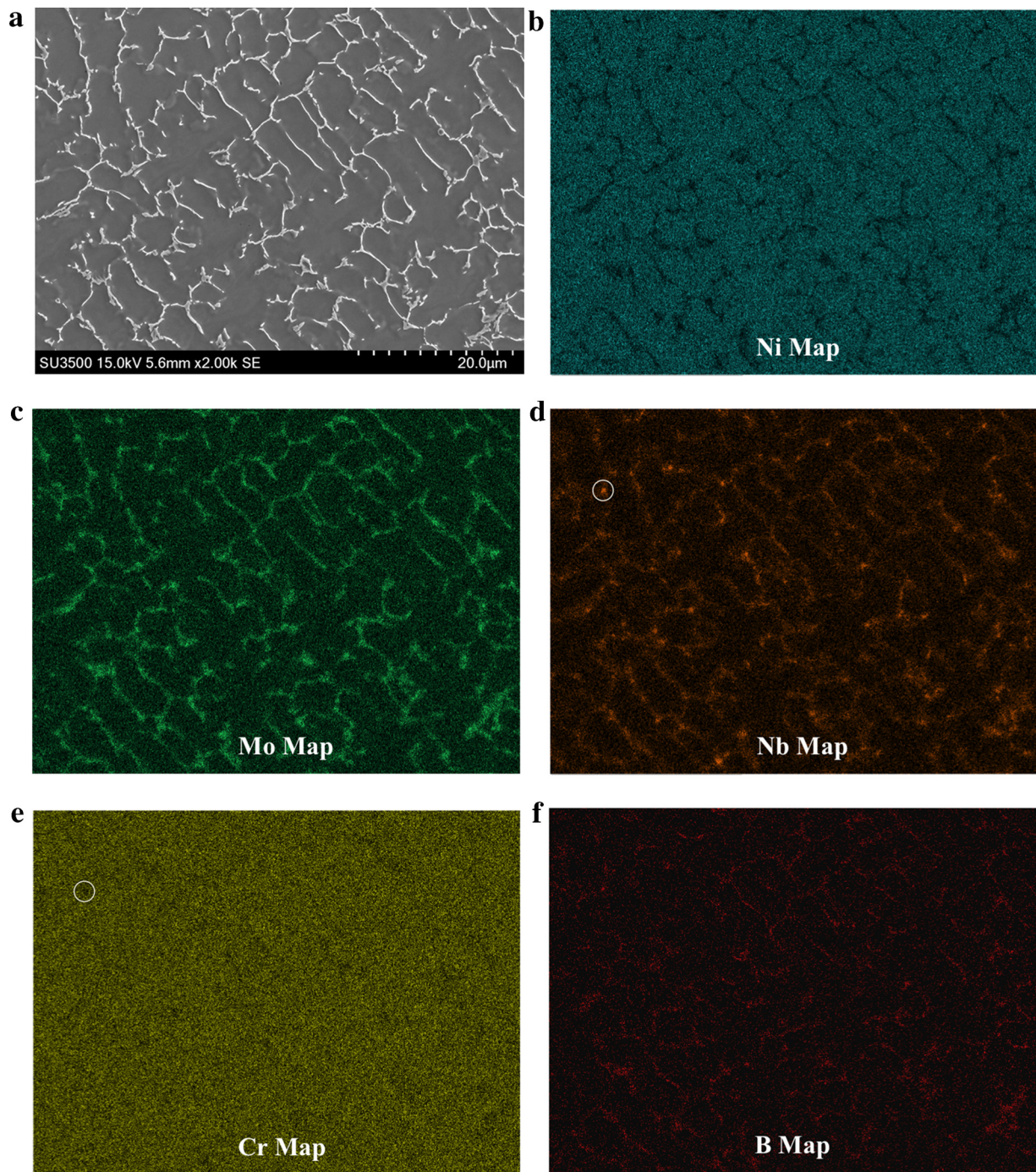
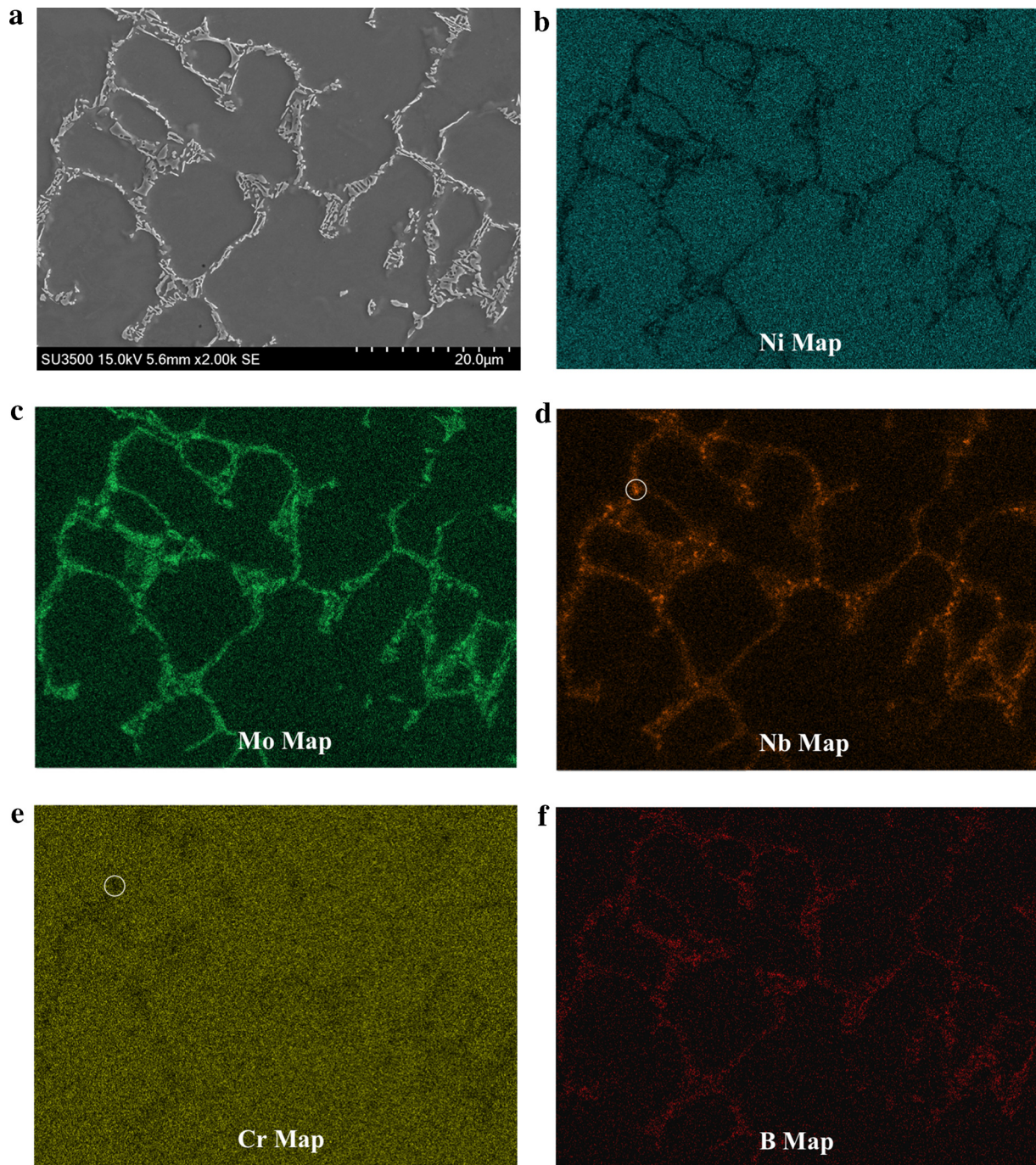


Fig. 3. a). SEM micrograph in the layer core showing continuous eutectic in inter-dendritic regions; EDS maps of b) Ni map; c) Mo map; d) Nb map; e) Cr map; f) B map. White circle represents NbC that composed of Nb and Mo, and depleted in Cr.

The samples obtained after deposition were sectioned along the transverse direction, followed by sequential grinding steps up to 800 grit using silicon carbide abrasive papers, and standard polishing steps were used up to 1  $\mu\text{m}$ . The polished samples were electrolytically etched in a solution of 12 ml  $\text{H}_3\text{PO}_4$  + 40 ml  $\text{HNO}_3$  + 48 ml  $\text{H}_2\text{SO}_4$  at 6 V for 5 s to reveal the microstructure [22]. The microstructure of the as-deposited samples were characterized using a Nikon optical light microscope with Clemex Vision System, a SU3500 scanning electron microscope (SEM) equipped for electron dispersive spectrometer (EDS) analysis. Interaction volumes of  $16 \mu\text{m}^3$  for EDS were calculated using Monte Carlo simulation from Casino [23]. Five different regions were chosen in order to measure the dendrite arm spacing using ImageJ

image analysis software [24] and the average results are presented in this discussion. According to the similar process of measuring grain size as per ASTM E112 [25], the dendrite arm spacing was measured manually by dividing the length of a line by the number of dendrites within the line. To measure the area fractions of eutectics, the micrographs contrast was enhanced in order to better differentiate between the eutectic phases and  $\gamma$  solid solution. This image processing technique allowed the proper delineation required for regular image analysis routine using ImageJ. The grain morphology and texture of the as-deposited samples were studied using electron backscattered diffraction (EBSD) equipped on the same SEM. The samples for EBSD were polished to 0.05  $\mu\text{m}$  in colloidal silica suspension. The Aztec data



**Fig. 4.** a). SEM micrograph in the layer boundary showing continuous eutectic in inter-dendritic regions; EDS maps of b) Ni map; c) Mo map; d) Nb map; e) Cr map; f) B map. White circle represents NbC that composed of Nb and Mo, and depleted in Cr.

acquisition software employed with the HKL Channel 5 data processing software was performed for the EBSD analysis. The microstructural analysis of the deposits in the lower region of the part and near the substrate were not considered in the presented work due to the high influence of dilution from the substrate.

### 3. Results and discussion

#### 3.1. Microstructure evolution

Fig. 2(a) is a representative optical macroscopic image of the deposit of 625B produced via the laser wire deposition process, the layer boundary can be clearly observed. The layer boundary, that formed due

to the re-melting of previous deposits and at the beginning of solidification, has the typical morphology of a laser melted layer-by-layer additively manufactured microstructure [20]. Fig. 2(b) depicts that the layer boundary has a thickness of around 250  $\mu\text{m}$ . Fig. 2(b) indicates a dendritic microstructure with a growth direction parallel to the building direction. It is understood that cooling in LAM occurs predominantly via heat transfer through the solidified deposits and the substrate. This results in the heat flow direction to be perpendicular to the substrate during melt pool solidification. This directional growth behavior during LAM processes has also been observed in previous studies [10,26].

An SEM micrograph of the transition between the layer core and layer boundary is highlighted in Fig. 2(c), with higher magnification

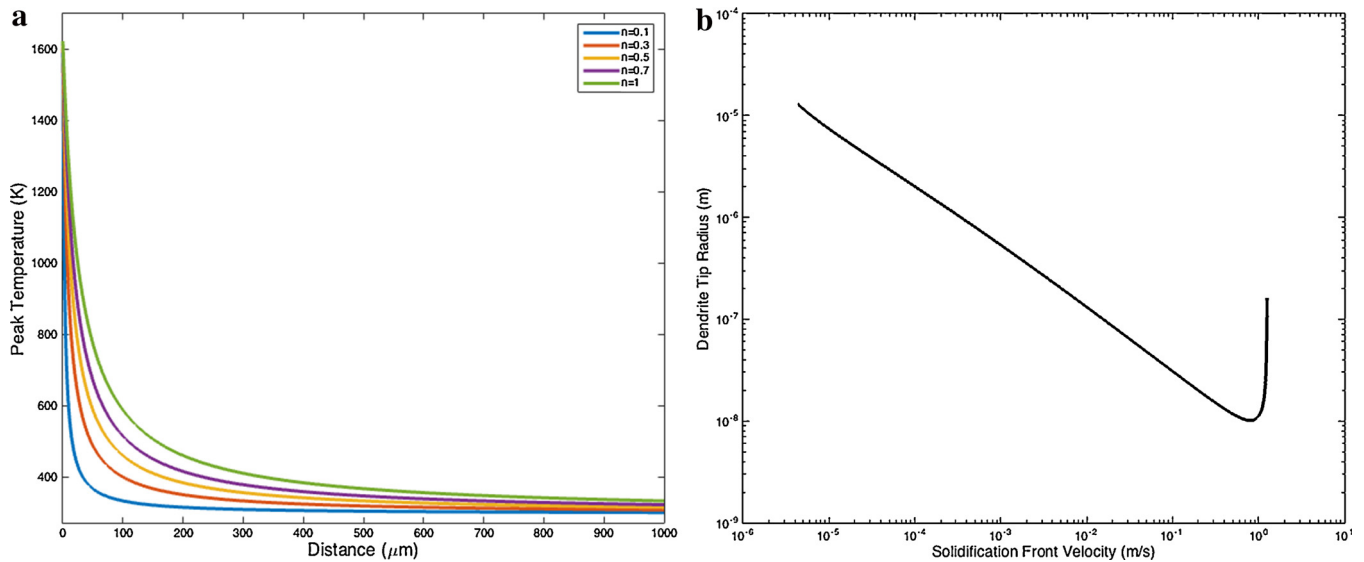


Fig. 5. (a). Temperature decay profile for various efficiencies during laser wire deposition solidification. (b) The KGT model describing the dendrite tip radius as a function of SFV.

micrographs shown in Fig. 2(d) and (e) for the layer core and layer boundary, respectively. As depicted, both the layer core and layer boundary display a dendritic structure and continuous eutectics segregating the inter-dendritic regions. However, the solidification features in the layer boundary were larger than those in the layer core. The coarsened features in the layer boundary have been attributed to the recalescence phenomena, meaning that the latent heat flow becomes retarded by the formation of the primary  $\gamma$  phase at the beginning of solidification, and the temperature gradient and cooling rate decreases accordingly, leading to the larger observed morphology. The coarsened morphology, due to the recalescence phenomena, has been noted before in the melt pool boundaries during pulsed SLM of Al-12%Si alloy [27].

The dendrite arm spacing (DAS) for the layer core and layer boundary were measured to be  $4.8 \pm 0.9 \mu\text{m}$  and  $7.2 \pm 1.2 \mu\text{m}$ , respectively. The area fractions of the eutectics in the layer core and layer boundary are  $8.6 \pm 1.3\%$  and  $7.4 \pm 1.5\%$ , respectively. Both eutectic values are significantly higher than the reported 2% measured for Alloy 625 after welding solidification [28] and measured 1.6%–2.3% for Alloy 625 after laser additive manufacturing [10,12,14], and are above the threshold to obtain crack-free builds in both the deposits and the substrate [26].

EDS maps of the main alloying elements (Ni, Mo, Nb, Cr and B) were collected to observe the elemental concentration of the different phases in the layer core, and are presented in Fig. 3. As depicted, the  $\gamma$  matrix was rich in Ni and Cr. The continuous eutectics in the inter-dendritic regions were mainly Laves phase with enrichment of Nb, Mo and B. A small portion of NbC was present composed of Nb and Mo, and depleted of Cr (highlighted in small circles in Fig. 3(d) and (e)). Laves phase is an intermetallic compound with the  $X_2Y$  type structure. In conventional IN625, X (including Ni and Cr) stands for the solid constituent, and Y (including Nb and Mo) represents the liquid constituent [17]. In the current study the addition of B, acting as a melting point depressant, would substitute in the liquid constituent (Y) and lead to an increase in the amount of Laves eutectics present during the final stage of solidification. The feasibility of this elemental substitution of B in Laves phase has been validated by previous work using density function theory (DFT) during gas tungsten arc deposition of 625B [19].

EDS maps of the same elements were acquired to analyze the elemental constitution of the different phases at the layer boundary, and the results are summarized in Fig. 4. The results depict the same phases with similar elemental constitutions in the layer boundary as the layer core. The  $\gamma$  matrix in the dendritic boundary was again, rich in Ni and

Cr. In the inter-dendritic region, the continuous eutectics consist of mainly Laves phases with a small amount of NbC. As previous discussed, the Laves phase present was enriched with Nb, Mo and B. The NbC was composed of Nb and Mo, and depleted of Cr (white circle in Fig. 4(d) and (e) highlight this observation).

### 3.2. Rapid solidification behavior

The temperature decay profile of one layer during laser wire deposition solidification was calculated using Adam's 2D equation expressed in Eq. (1) [29]

$$\frac{1}{T_p - T_0} = \frac{4.13VYg\rho C}{Q} + \frac{1}{T_m - T_0} \quad (1)$$

Where  $T_p$  is the temperature at a given position,  $T_0$  is the initial temperature of the deposits,  $T_m$  is the melting temperature of the deposits,  $g$  is the workpiece thickness and in this case treated as constant,  $V$  is the scanning velocity relative to the substrate,  $Y$  is the distance from the center of the laser spot,  $\rho$  is the density,  $C$  is the specific heat of the workpiece, and  $Q$  is the energy input of the deposition process. The values of  $T_0 = 293 \text{ K}$  ( $25^\circ\text{C}$ ),  $T_m = 1623 \text{ K}$  ( $1350^\circ\text{C}$ ),  $\rho = 8.44 \text{ g/cm}^3$  and  $C = 410 \text{ J/(Kg.K)}$  were used in this calculation. The energy input is expressed in Eq. (2):

$$Q = nP_L \quad (2)$$

Where  $P_L$  is the laser beam power, and  $n$  is the efficiency of the deposition process with variation from 0.1 to 1.

The results are presented in Fig. 5(a) for the laser wire deposition process with different efficiencies. The results show that temperature decay to ambient conditions was within 1 mm relative to the center of the laser spot. According to Saepen and Turnbull [30], for metal alloys, the local liquid-solid interfacial morphology was considered to be significant if the ambient temperature was reached within a distance of 1 mm. Thus, highlighting the importance of the relationship between laser wire deposition solidification and interfacial morphology development.

The Kurz-Giovanolva and Trivedi (KGT) model [31] was developed to describe the solid-liquid interfacial morphology variation during rapid solidification. In this work we have applied it to obtain the relationship between the dendrite tip radius and the solidification front velocity (SFV). The KGT model considers the solid-liquid interfacial stabilization with changing surface tension during rapid solidification

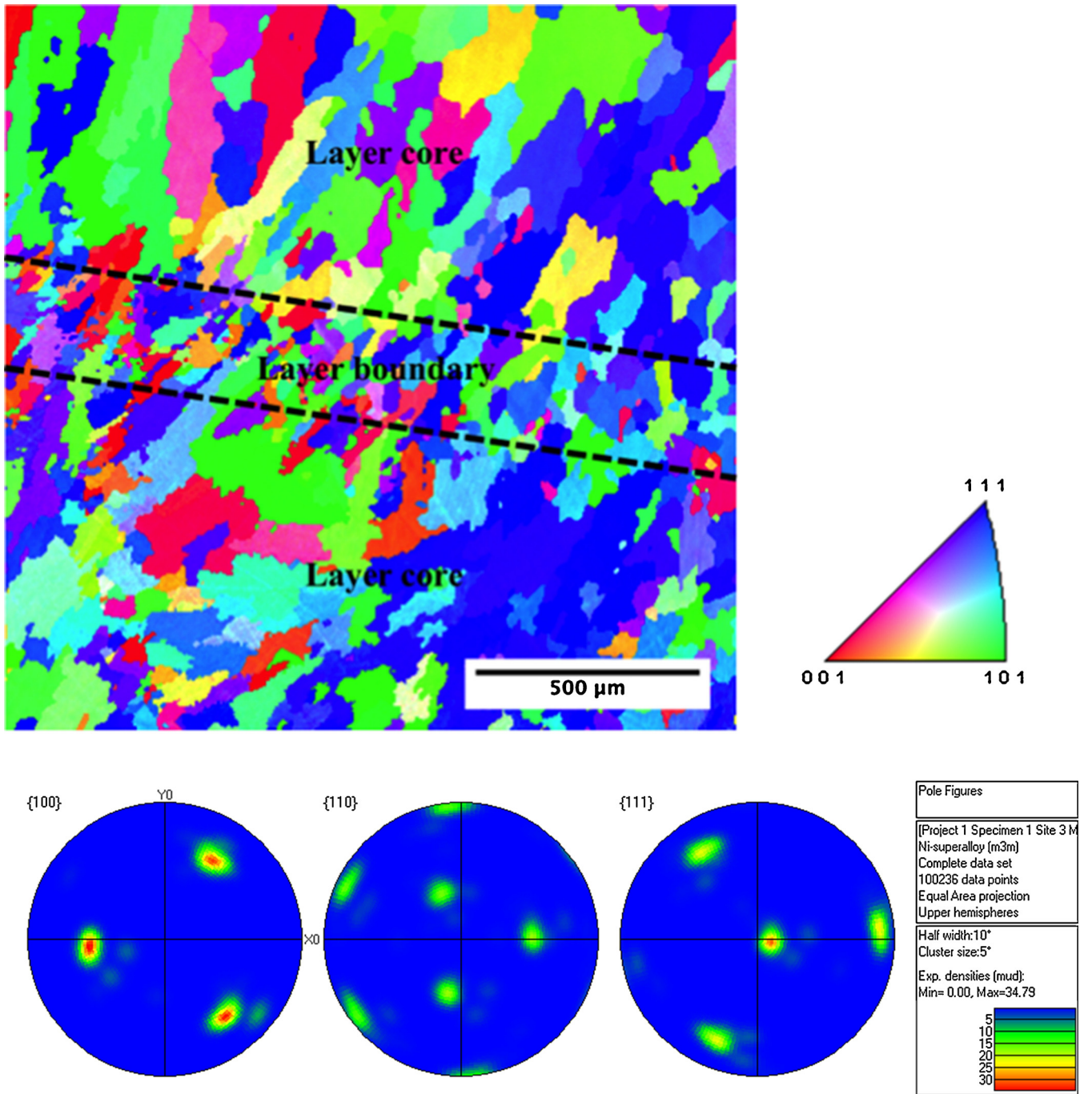


**Fig. 6.** a) EBSD map of as-deposited sample (with coloured orientation image map) showing small equiaxed grains in the layer boundary and columnar grains prevailing in the layer core; b) Pole figures of as-deposited sample showing strong texture along (100) planes.

under high SFV. The NiCr-B system was selected to study the KGT model in the current case [26]. The KGT model is expressed in Eq. (3),

$$R = 2\pi \left[ \frac{\Gamma}{mG_c \xi_c - G} \right]^{1/2} \quad (3)$$

where  $R$  is the dendrite tip radius. Based on Kurz and Fisher model [32] for estimation of dendrite tip radius as a function of DAS,  $R$  is calculated to be about 30 nm and 50 nm for the layer core and layer boundary, respectively.  $\Gamma$  is the Gibbs-Thompson coefficient and is estimated as  $3.42 \times 10^{-7}$  Km for Ni-B system during rapid solidification [33],  $m$  is the slope of the liquidus line in the phase diagram,  $G_c$  is the concentration gradient of the solute at the liquid-solid interface and is

determined through the mass balance across the dendrite tip,  $G$  is the mean temperature gradient at the interface and is estimated to be  $10^6$  Km using thermal decay profile as shown in Fig. 5(a).

The parameter  $\xi_c$  in KGT model is expressed in Eq. (4)

$$\xi_c = 1 - \frac{2k}{[1 + (2\pi/P)^2]^{1/2} - 1 + 2k} \quad (4)$$

Where  $P$  is the Péclet number,  $k$  is the partition coefficient and has a value of 0.008 for B in  $\gamma$ -Ni [34].

The numerically calculated KGT is presented in Fig. 5(b). As depicted, the dendrite tip radius of 30 nm and 50 nm yield SFV values of around 0.1 m/s and 0.06 m/s for the layer core and layer boundary, respectively. It is indicated from Fig. 5(b) that at high SFV with a value

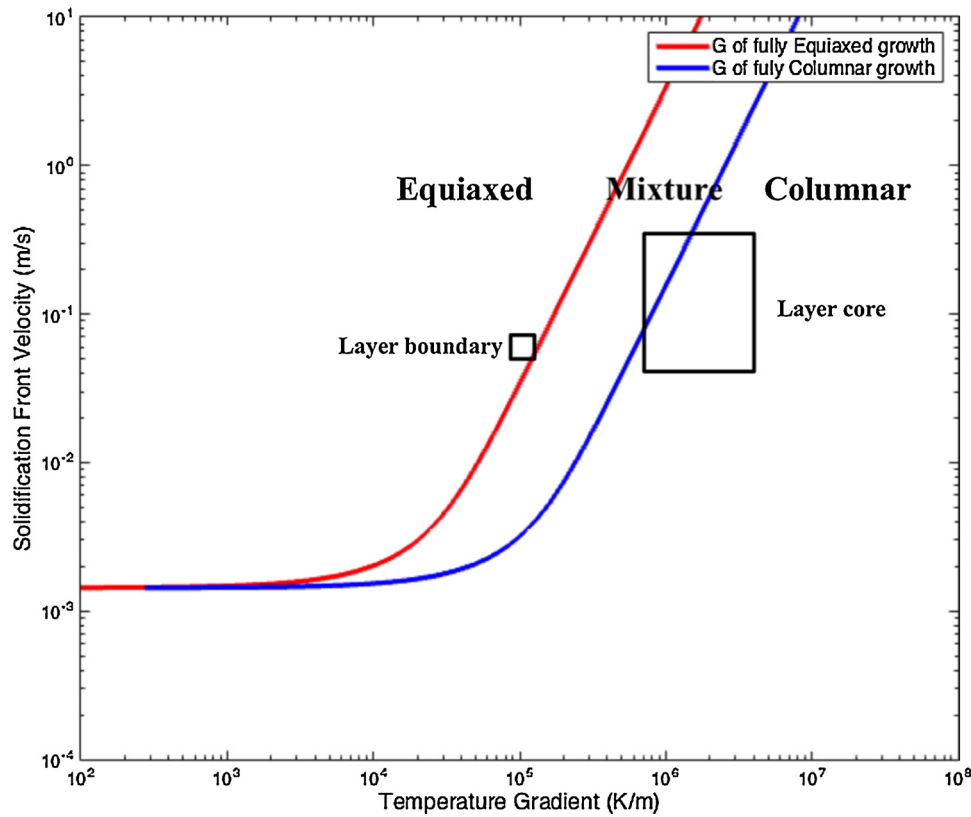


Fig. 7. CET model showing equiaxed grains in the layer boundary and columnar grains in the layer core.

over 1 m/s, the planar feature would be obtained as no dendrite tip would be formed. With a SFV of around 1 m/s, the planar interface would break down to a cellular morphology with smallest tip radius. When the SFV is smaller than 1 m/s, the cellular interface would transform to a dendritic microstructure [31]. The solidification mode, predicted from the calculated SFV, suggests that a dendritic structure will form in both the layer core and the layer boundary, which was supported by the experimental observations.

### 3.3. Grain morphology

EBSM map was acquired to observe the grain morphology, and a representative micrograph is presented in Fig. 6. Fig. 6(a) shows that small equiaxed  $\gamma$  grains occupy the layer boundary, while large columnar  $\gamma$  grains with a small portion of equiaxed grains were present in the layer core. The thickness of the layer boundary was around 250  $\mu\text{m}$  and was consistent with the observations shown in Fig. 2(a). The equiaxed grains found in the layer boundary is the opposite to the typical epitaxial growth that is reported along the building direction of Nb-bearing superalloys fabricated by LAM [10,35,36]. Previous reports have shown that only columnar  $\gamma$  grains have been observed and were detrimental to the mechanical properties of the material along the deposition direction. The corresponding pole figures are displayed in Fig. 6(b). The pole figures highlight a strong texture orientation along (100) planes which has been reported before in LAM of Ni-based superalloys [35,36].

The columnar to equiaxed transition (CET) model developed by Hunts [37] was applied to explain the observed grain morphology in Fig. 6(a), the result are shown in Fig. 7. In order to predict the solidification mode in different regions, the temperature gradient in the layer boundary is required. The relationship between primary DAS, the temperature gradient and SFV is expressed by Eq. (5) [38]

$$\lambda = Av^{-0.25}G^{-0.5} \quad (5)$$

Where  $\lambda$  is the DAS,  $A$  is material constant. The mean temperature gradient in the layer boundary can be estimated to be in the magnitude of  $10^5$  K/m.

The solidification path regimes for the layer boundary and the layer core were then predicted in Fig. 7. It is worth noting that, within the layer core the temperature gradient is higher and solidification rate is lower near the boundary than the inner regions [29]. This results in a larger solidification path region for the layer core. As depicted in Fig. 7, the solidification mode prediction for the layer boundary is almost fully equiaxed grain growth. According to Thompson and Spaepen [39], as a melting point depressant element, B could decrease the viscosity of the liquid at initial solidification. The reduced viscosity would decrease the surface tension and improve the wettability of the system resulting in more heterogeneous nucleation sites [40]. The increased number of nucleation sites favors equiaxed grain nucleation and growth, which was observed in the layer boundary [40]. This mechanism becomes more pronounced as solidification progressed due to the very low partition coefficient of B in  $\gamma$ -Ni. Therefore, the B addition have shown to help increase heterogeneous nucleation sites during solidification and results in the formation of equiaxed grains as the dominant solidification mode in the layer boundary. Even with the addition of B to the Alloy 625 composition, the solidification morphology of the layer core was predominantly columnar with a small portion of equiaxed growth according to the calculated solidification path regime. This predicted was consistent with finding from the EBSM map shown in Fig. 6a.

## 4. Conclusion

The inclusion of 0.4 wt% boron into Alloy 625 results in the production of a significantly higher volume fraction of eutectics in laser wire deposition. The eutectics consist of mainly Laves phase with a small number of NbC precipitates. The increased volume of eutectics was sufficient to backfill the solidification defects and support the

concept of using B-modified Alloy 625 to prevent issues associated with hot cracking during laser wire deposition. The layer boundary with a coarsened microstructure was formed and associated with the recalescence phenomena. From the KGT model, SFV in the layer boundary and layer core were calculated to be 0.06 m/s and 0.1 m/s, respectively. Full equiaxed grain growth was found in the layer boundary, which deviates from the typical epitaxial growth mode of additively manufactured Ni-based superalloys. In the layer core, the solidified structure was dominated by columnar growth with a few equiaxed grains. This solidification mode was simulated using the CET model to rationalize the observed grain morphology.

### Acknowledgement

The authors would like to acknowledge the financial support from NSERC through the CRD-331023745 awarded grant. We would also like to thank McGill Engineering Doctoral Award (MEDA) for the PhD scholarship granted to Mr. Tian.

### References

- [1] M.J. Cieslak, The welding and solidification metallurgy of Alloy 625, *Weld. J.* 70 (1991) 49s–56s.
- [2] J.J. Valencia, J. Spirko, R. Schmees, E.A. Loria (Ed.), *Superalloys 718, 625, 706 and Various Derivates*, TMS, Warrendale, PA, 1997, pp. 753–762.
- [3] E. Pavithra, V.S. Senthil Kumar, microstructural evolution of hydroformed inconel 625 bellows, *J. Alloys. Compd.* 669 (2016) 199–204.
- [4] L. Thivillon, P. Bertrand, B. Laget, I. Smurov, Potential of direct metal deposition technology for manufacturing thick functionally graded coatings and parts for reactors components, *J. Nucl. Mater.* 385 (2) (2009) 236–241.
- [5] A. Theriault, L. Xue, J.R. Dryden, Fatigue behavior of laser consolidated IN-625 at room and elevated temperatures, *Mater. Sci. Eng. A* 516 (1–2) (2009) 217–225.
- [6] K.H. Song, K. Nakata, Effect of precipitation on post-heat-treated Inconel 625 alloy after friction stir welding, *Mater. Des.* 31 (6) (2010) 2942–2947.
- [7] P. Ganesh, R. Kaul, C.P. Paul, P. Tiwari, S.K. Rai, R.C. Prasad, L.M. Kukreja, Fatigue and fracture toughness characteristics of laser rapid manufactured Inconel 625 structures, *Mater. Sci. Eng. A* 527 (29–30) (2010) 7490–7497.
- [8] X. Xing, X. Di, B. Wang, The effect of post-weld heat treatment temperature on the microstructure of Inconel 625 deposited metal, *J. Alloys. Compd.* 593 (0) (2014) 110–116.
- [9] A. Ascari, A. Fortunato, A.H.A. Lutey, G. Guerrini, N. Pagano, Long pulse laser wire deposition of hard steels, *Phys. Procedia* 83 (2016) 723–732.
- [10] G.P. Dinda, A.K. Dasgupta, J. Mazumder, Laser aided direct metal deposition of Inconel 625 superalloy: microstructural evolution and thermal stability, *Mater. Sci. Eng., A* 509 (1–2) (2009) 98–104.
- [11] T.E. Abioye, J. Folkles, A.T. Clare, A parametric study of Inconel 625 wire laser deposition, *J. Mater. Process. Technol.* 213 (12) (2013) 2145–2151.
- [12] T.E. Abioye, D.G. McCartney, A.T. Clare, Laser cladding of Inconel 625 wire for corrosion protection, *J. Mater. Process. Technol.* 217 (0) (2015) 232–240.
- [13] J.C. Heigel, P. Michaleris, T.A. Palmer, In situ monitoring and characterization of distortion during laser cladding of Inconel® 625, *J. Mater. Process. Technol.* 220 (0) (2015) 135–145.
- [14] S. Li, Q. Wei, Y. Shi, Z. Zhu, D. Zhang, Microstructure characteristics of inconel 625 superalloy manufactured by selective laser melting, *J. Mater. Sci. Technol.* 31 (9) (2015) 946–952.
- [15] K. Banerjee, N.L. Richards, M.C. Chaturvedi, Effect of filler alloys on heat-affected zone cracking in preweld heat-treated IN-738 LC gas-tungsten-arc welds, *MMTA* 36 (7) (2005) 1881–1890.
- [16] D. Liu, J. Lippold, J. Li, S. Rohklin, J. Vollbrecht, R. Grylls, Laser engineered net shape (LENS) technology for the repair of Ni-Base superalloy turbine components, *MMTA* 45 (10) (2014) 4454–4469.
- [17] J.N. DuPont, J.C. Lippold, S.D. Kiser, *Welding Metallurgy and Weldability of Nickel-base Alloys*, (2009) <http://www.books24x7.com/marc.asp?bookid=33735>.
- [18] B. Alexandrov, A. Hope, J. Sowards, J. Lippold, S. McCracken, *Weldability Studies of High-Cr, Ni-Base filler metals for power generation applications*, *Weld World* 55 (3–4) (2011) 65–76.
- [19] Y. Tian, B. Ouyang, A. Gontcharov, R. Gauvin, P. Lowden, M. Brochu, Microstructure evolution of Inconel 625 with 0.4 wt% boron modification during gas tungsten arc deposition, *J. Alloys. Compd.* 694 (2017) 429–438.
- [20] Y. Tian, D. McAllister, H. Colijn, M. Mills, D. Farson, M. Nordin, S. Babu, Rationalization of microstructure heterogeneity in INCONEL 718 builds made by the direct laser additive manufacturing process, *MMTA* 45 (10) (2014) 4470–4483.
- [21] J.-z. Su, M.-z. Xiao, Z.-j. Zhang, Z.-p. Ye, X. Jin, Y.-c. Yang, Microstructural morphology and evolution of austenite stainless steel deposited using pulsed laser and wire, *Int. J. Adv. Manuf. Technol.* 93 (9) (2017) 3357–3370.
- [22] Y. Tian, A. Gontcharov, R. Gauvin, P. Lowden, M. Brochu, Effect of heat treatments on microstructure evolution and mechanical properties of blended nickel-based superalloys powders fabricated by laser powder deposition, *Mater. Sci. Eng. A* 674 (2016) 646–657.
- [23] D. Drouin, A.R. Couture, D. Joly, X. Tastet, V. Aimez, R. Gauvin, CASINO V2.42—a fast and easy-to-use modeling tool for scanning Electron microscopy and microanalysis users, *Scanning* 29 (3) (2007) 92–101.
- [24] C.A. Schneider, W.S. Rasband, K.W. Eliceiri, *Nat. Methods* 9 (2012) 671–675.
- [25] A. E1951, *Standard Guide for Calibrating Reticles and Light Microscope Magnifications*, 2014 Edition.
- [26] Y. Tian, R. Gauvin, M. Brochu, Microstructure evolution and rapid solidification behavior of blended nickel-based superalloy powders fabricated by laser powder deposition, *MMTA* 47 (7) (2016) 3771–3780.
- [27] R. Chou, J. Milligan, M. Paliwal, M. Brochu, Additive manufacturing of Al-12Si alloy via pulsed selective laser melting, *Jom* 67 (3) (2015) 590–596.
- [28] J.N. DuPont, Solidification of an alloy 625 weld overlay, *MMTA* 27 (11) (1996) 3612–3620.
- [29] S. Kou, *Heat Flow in Welding*, Welding Metallurgy, John Wiley & Sons, Inc, 2003, pp. 37–64.
- [30] F. Spaepen, D. Turnbull, Chapter 2 - crystallization processes, in: J.M.P.W. Mayer (Ed.), *Laser Annealing of Semiconductors*, Academic Press, 1982, pp. 15–42.
- [31] W. Kurz, B. Giovanola, R. Trivedi, Theory of microstructural development during rapid solidification, *Acta Metall.* 34 (5) (1986) 823–830.
- [32] W. Kurz, D.J. Fisher, Dendrite growth at the limit of stability: tip radius and spacing, *Acta Metall.* 29 (1) (1981) 11–20.
- [33] K. Eckler, D.M. Herlach, M.J. Aziz, Search for a solute-drag effect in dendritic solidification, *Acta Metall. Mater.* 42 (3) (1994) 975–979.
- [34] O.A. Ojo, N.L. Richards, M.C. Chaturvedi, Study of the fusion zone and heat-affected zone microstructures in tungsten inert gas-welded INCONEL 738LC superalloy, *MMTA* 37 (2) (2006) 421–433.
- [35] L.E. Murr, E. Martinez, S.M. Gaytan, D.A. Ramirez, B.I. Machado, P.W. Shindo, J.L. Martinez, F. Medina, J. Wooten, D. Ciscel, U. Ackelid, R.B. Wicker, Microstructural Architecture, Microstructures, and Mechanical Properties for a Nickel-Base Superalloy Fabricated by Electron Beam Melting, *MMTA* 42 (11) (2011) 3491–3508.
- [36] L.L. Parimi, G.A. Ravi, D. Clark, M.M. Attallah, Microstructural and texture development in direct laser fabricated IN718, *Mater. Charact.* 89 (2014) 102–111.
- [37] J.D. Hunt, Steady state columnar and equiaxed growth of dendrites and eutectic, *Mater. Sci. Eng.* 65 (1) (1984) 75–83.
- [38] E. Çadırli, İ. Karaca, H. Kaya, N. Maraşlı, Effect of growth rate and composition on the primary spacing, the dendrite tip radius and mushy zone depth in the directionally solidified succinonitrile–Salol alloys, *J. Cryst. Growth* 255 (1–2) (2003) 190–203.
- [39] C.V. Thompson, F. Spaepen, Homogeneous crystal nucleation in binary metallic melts, *Acta Metall.* 31 (12) (1983) 2021–2027.
- [40] B.S. Murty, S.A. Kori, M. Chakraborty, Grain refinement of aluminium and its alloys by heterogeneous nucleation and alloying, *Int. Mater. Rev.* 47 (1) (2002) 3–29.